A porous circulation model of the human brain for *in silico* clinical trials in ischaemic stroke

Józsa, T. I.*[1], Padmos, R. M.[2], Samuels, N.[3], El-Bouri, W. K.[1], Hoekstra, A. G.[2], and Payne, S. J.[1]

[1]Institute of Biomedical Engineering, Department of Engineering Science, University of Oxford, Parks Road, Oxford OX1 3PJ, UK
[2]Computational Science Laboratory, Institute for Informatics, Faculty of Science, University of Amsterdam, Science Park 904, Amsterdam 1098 XH, the Netherlands
[3]Department of Radiology and Nuclear Medicine, Erasmus MC, University Medical Center, Rotterdam 3015 GD, the Netherlands

Abstract

The advancement of ischaemic stroke medication and treatment relies on resource-intensive experiments and clinical trials. In order to improve thrombolysis and thrombectomy, we target the development of computational tools for *in silico* trials which can partially replace these animal and human experiments with fast simulations. This study proposes a model that will serve as part of a predictive unit estimating patient outcome as a function of treatment. In particular, the present work aims at the development and evaluation of an organ-scale microcirculation model of the human brain for perfusion prediction. The model relies on a three-compartment porous continuum approach. Firstly, a fast and robust method is established to compute the anisotropic and inhomogeneous permeability tensors representing arterioles and venules. Secondly, vessel-encoded arterial spin labelling and clustering are employed to create a unique and anatomically accurate mapping between the microcirculation and large arteries. Thirdly, the parameter space of the problem is reduced by analysing the governing equations and experimental data. Fourthly, a parameter optimisation is conducted. Finally, simulations are performed with the tuned model to obtain perfusion maps corresponding to an open and an occluded (ischaemic stroke) scenario. The perfusion map in the occluded vessel scenario shows promising qualitative agreement with CT images. In the future, the model will be thoroughly validated against experiments.

*Corresponding author: Tamás István Józsa, tamas.jozsa@eng.ox.ac.uk

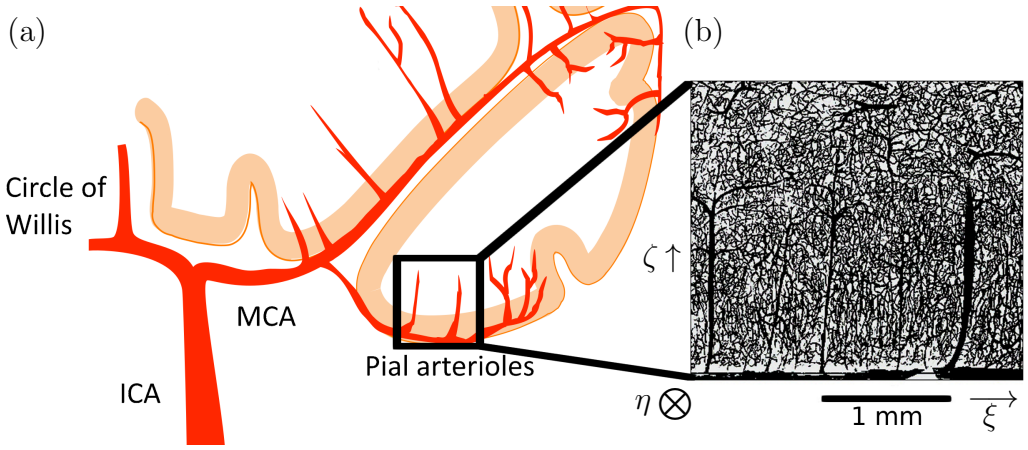

Figure 1: Structure of the brain vasculature: (a) schematic drawing of the large arteries including the Internal Carotid Artery (ICA) and the Middle Cerebral Artery (MCA). Adapted from the work of Iadecola [7]. (b) structure of the human cerebral mircovasculature visualised with india ink under confocal laser microscopy. Modified with permission from Cassot *et al.* [8]. The reference coordinate system (ξ, η, ζ) is shown in (b).

1 Introduction

In recent decades, ischaemic stroke treatment has been revolutionised by thrombolysis (the dissolving of blood clot) [1] and thrombectomy (the mechanical removal of clot) [2, 3]. Consequently, the survival rate of stroke patients has increased [4]. When successful, both thrombolysis and thrombectomy restore blood flow in the previously blocked vessels (recanalisation). However, it has been reported that even after recanalisation, blood flow to the tissue downstream to the occluded artery (perfusion) is often not or only partially recovered and hence brain tissue loss continues [1]. The mortality rate of patients after intervention is still relatively high [5]. In addition, a substantial proportion of the survivors (25–74%) suffer from a severe loss of congnitive function [6]. Taking care of functionally dependent patients imposes a heavy burden on society, both economically and mentally [5].

Regarding the poor outcome of ischaemic stroke patients, it is recognised that certain mechanisms can limit perfusion restoration. For instance, during thrombectomy or thrombolysis, the clot (thrombus) is not perfectly removed or disolved. Therefore, a cloud of clot fragments (emboli) can be released to the blood stream during treatment [9]. It has been hypothesised that when emboli reach the microcirculation, they cause micro-occlusions, and hence prevent reperfusion [10]. Another important mechanism is oedema, during which swelling of the brain deforms the tissue and alters blood pressure [11]. In order to maximise the positive outcome of treatments, such hypotheses have to be carefully investigated and counteracting interventions have to be worked out. The advancement and further development of related drugs and devices rely on resource-intensive and time-consuming pre-clinical animal experiments and clinical studies. Unfortunately, the success rate of medication that passes pre-clinical testing is low because the human brain behaves very differently from cell cultures or animal brains [12].

The INSIST (*IN Silico* clinical trials for treatment of acute Ischaemic STroke) consortium (www.insist-h2020.eu) set out to accelerate the advancement of human ischaemic stroke treatments by introducing *in silico* clinical trials which mitigate the need for resource-intensive experiments. INSIST promotes the application of computational methods for pharmacology and medical device development, which aligns with the ambitions of the Virtual Physiological Human (VPH) initiative [13]. This study contributes to INSIST and the VPH by developing a cerebral microcirculation model for the entire human brain, which is capable of predicting perfusion before and after an ischaemic stroke. This model will be coupled to a one-dimensional blood

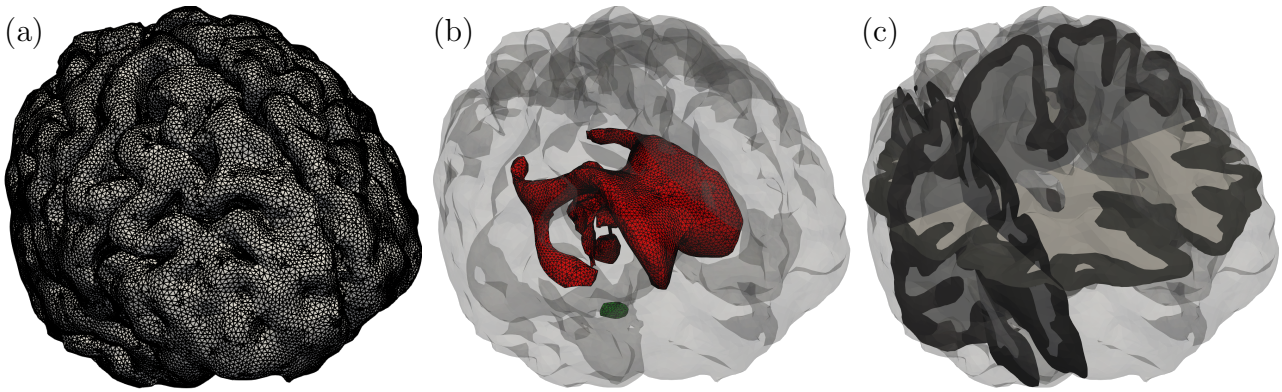

Figure 2: Computational domain and mesh: (a) the pial surface; (b) ventricles (red) and the cut-plane of the brainstem (green); subdomains including grey and white matters visualised along a coronal, a sagittal and a transverse plane.

flow simulator governing blood flow in arteries supplying blood to the pial surface [14, 15]. The role of the resulting organ-scale cerebral blood flow model in the *in silico* clinical trial will be to evaluate the impact of stroke treatment (thrombectomy or thrombolysis) on tissue perfusion. Furthermore, the model will provide input to other models which describe oxygen transport and infarct progression in the brain. The envisioned software suite will predict the outcome of ischaemic stroke treatment on a population level, provide guidance for objective clinical decision making, and lead to further drug and medical device development.

Progress in the mathematical and computational modelling of the cerebral circulation is complicated by the multi-scale nature of the flow and related transport processes. The diameter of blood vessels stretches from approximately 5 millimetres to 5 microns, being characteristic of the internal carotid artery and the capillaries, depicted in Figures 1(a) and (b) respectively. Cortical columns (with volumes of a few cubic millimetres) have been modelled by treating the capillary bed as a porous medium [16] and representing the connecting arterioles and venules as a one-dimensional vessel network [17, 18]. Scaling such models to the entire brain is computationally resource intensive, because it requires capturing the flow in the corresponding large networks of arterioles and venules. Nevertheless, with simplifications regarding the vessel networks, this approach has been successfully employed to investigate the temperature regulation of the human brain [19]. To overcome difficulties originating from the large networks, a two-compartment porous continuum model has been implemented for the human brain [20] where the arteriole and venule compartments include the majority of the small vessels. These models are reminiscent of heart perfusion models [21, 22, 23].

The present study sets out to investigate the capabilities of porous continuum models in terms of estimating the perfusion changes in various brain territories as a result of major vessel occlusion. To this end, we aim to improve the recently introduced organ-scale cerebral microcirculation models [19, 20]. As shown in Figures 1(a) and (b), the descending arterioles (and ascending veins) originating from the pial vessels are oriented perpendicularly to the cortical surface. The continuum representation of such networks requires heterogeneous and anisotropic permeability fields [21, 22, 23] which have been disregarded in previous studies for simplicity [19, 20]. It has been demonstrated that capturing such spatial variation in the properties of the continuum models plays an important role in the description of organ-scale physiological processes [24, 25].

Firstly, a robust algorithm will be presented which accounts for the heterogeneity and anisotropy of the human microcirculation. Thanks to brain atlases [26] and medical imaging technologies, such as Vessel-Encoded Arterial Spin Labelling (VE-ASL) [27, 28], it is now well-known that large vessels perfuse specific brain regions. Modelling the connections between

large vessels and their corresponding territories is crucial to predict the brain regions that are influenced by large vessel occlusion. In former studies [19, 20], the volume sources that coupled the one-dimensional networks and the porous continuum were not designed to incorporate these features. Secondly, an anatomically accurate mapping will be introduced between the micro and macro scales. Thirdly, we will parametrise the resulting porous continuum model and conduct optimisation to determine the unknown parameters. Finally, simulations will be reported which are capable of producing perfusion maps in healthy and occluded (ischaemic stroke) scenarios.

2 Methods

When considering organ-scale perfusion models, it is becoming common practice to use one-dimensional network models (for instance, [29, 30, 31, 32, 33]) for large arteries and multi-compartment porous continuum models for the microcirculation [19, 20, 21, 22, 23]. The microcirculation model proposed here builds on the same principles.

2.1 Computational domain and mesh

The computational domain (Ω) is a patient-specific human brain utilised in multiple recent studies [25, 34, 35]. The bounding surface regions ($\partial\Omega$) include a transverse cut-plane of the brainstem Γ_{BS}, the ventricles Γ_V and the pial surface Γ_P so that $\partial\Omega = \Gamma_{BS} \cup \Gamma_V \cup \Gamma_P$. These surface regions are depicted in Figures 2(a) and (b). Grey matter (Ω_G) and white matter (Ω_W) are visible along a transverse, a coronal and a sagittal plane in Figure 2(c). Our investigations are restricted to these two subdomains, therefore $\Omega = \Omega_G \cup \Omega_W$. The geometry is discretised on a tetrahedral mesh using Tetgen [36]. The mesh depicted in Figure 2 includes 1,042,301 elements.

The boundary region associated with the pial surface (Figure 2(a)) is subdivided into eight perfusion territories corresponding to major feeding arteries which have been identified with VE-ASL [27, 37, 38, 28, 39]. To this end, the same clustering algorithm is used as in our preliminary study [40] as detailed in [14, 15]. In the future, subdividing the pial surface into more sections will enable us to establish a feedback between the porous microcirculation model and a one-dimensional network model [14, 15] by the repeated refreshment of the boundary conditions. Each perfusion territory corresponds to a major feeding artery of the brain. These territories are identified based on VE-ASL images [39]. Thereafter, the surface region that is perfused, for instance, by the Right Middle Cerebral Artery (R-MCA) is denoted as $\Gamma_{\text{R-MCA}}$. This approach leads to an anatomically accurate coupling by ensuring that blood arrives to the brain tissue through specific cortical surface regions as shown in Figures 3(a), (b) and (c).

2.2 Governing equations and boundary conditions

The governing equations describing three porous compartments [21, 22, 23] are

$$\nabla \cdot (\boldsymbol{K_a} \nabla p_a) - \beta_{ac}(p_a - p_c) = 0; \tag{1a}$$

$$\nabla \cdot (\boldsymbol{K_c} \nabla p_a) + \beta_{ac}(p_a - p_c) - \beta_{cv}(p_c - p_v) = 0; \tag{1b}$$

$$\nabla \cdot (\boldsymbol{K_c} \nabla p_a) + \beta_{cv}(p_c - p_v) = 0. \tag{1c}$$

Here, p_a, p_c and p_v are the Darcy pressures corresponding to the arteriole, capillary and venule compartments respectively. $\boldsymbol{K_i}$ is the permeability tensor of compartment i, whereas β_{ij} denotes the coupling coefficients between compartments i and j. It is worth mentioning that a similar two-compartment (arteriole and venule) brain perfusion model has been reported recently [20]. Here, a three-compartment model is proposed because some relevant physiological

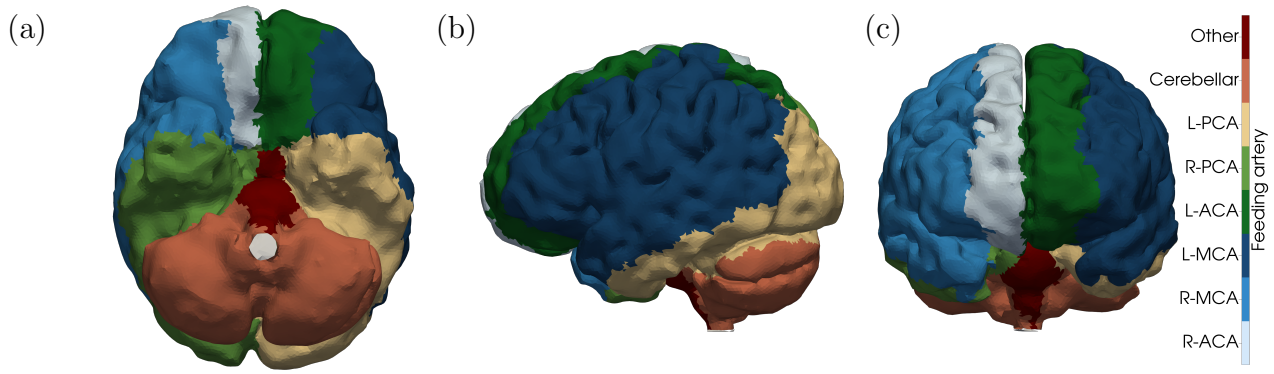

Figure 3: Superficial perfusion territories of large arteries projected onto the brain surface using the algorithm presented in [14, 15] and VE-ASL images [39]: (a) transverse view; (b) sagittal view; (c) coronal view. Territories corresponding to the Left and Right (L & R) hemispheres are labelled separately. Surface regions are coloured based on the feeding arteries using the following acronyms: Anterior Cerebral Artery (ACA), Middle Cerebral Artery (MCA), Posterior Cerebral Artery (PCA).

and biochemical processes are restricted to certain length scales. For instance, oxygen exchange through the blood brain barrier is most intensive in the capillary compartment. Furthermore, cerebral autoregulation mechanisms are different in arterioles and capillaries and seem to be absent in venules [41, 42, 43].

The boundary conditions imposed with equation (1) are as follows. Flow through the transverse cut-plane of the brainstem and the ventricles is zero in every compartment. Using $\boldsymbol{n}$ as the outward-pointing normal unit vector corresponding to the boundary surface, this Neumann boundary condition reads as

$$\boldsymbol{K_i} \nabla p_i \cdot \boldsymbol{n} = 0 \quad \text{on } \Gamma_{BS} \text{ and } \Gamma_V. \tag{2}$$

Flow through the pial surface in the capillary compartment is zero:

$$\boldsymbol{K_c} \nabla p_c \cdot \boldsymbol{n} = 0 \quad \text{on } \Gamma_P. \tag{3}$$

The zero level of pressure can be selected freely because of the incompressible fluid flow model. By setting the zero level of pressure on the pial surface in the venous compartment, the value of the venous pressure is eliminated from the model:

$$p_v = 0 \quad \text{on } \Gamma_P. \tag{4}$$

In the healthy scenario, the pressure on the pial surface in the arteriole compartment is the systolic pressure (p_{sys}):

$$p_a = p_{\text{sys}} \quad \text{on } \Gamma_P. \tag{5}$$

To account for occluded scenarios, the surface pressure associated with the perfusion territory of an occluded vessel is decreased to the venous pressure. Accordingly, the Dirichlet boundary conditions corresponding to a R-MCA occlusion become

$$p_a = 0 \quad \text{on } \Gamma_{\text{R-MCA}}, \text{ and} \tag{6a}$$

$$p_a = p_{\text{sys}} \quad \text{on } \Gamma_P \setminus \Gamma_{\text{R-MCA}}. \tag{6b}$$

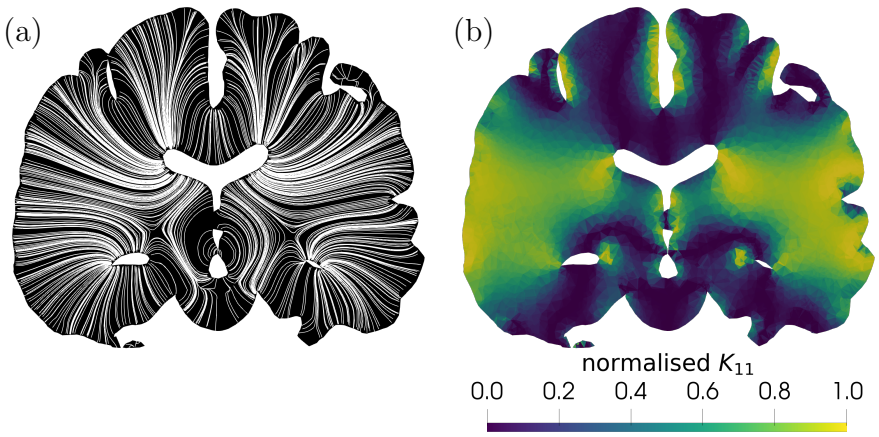

Figure 4: Tangent lines of the $\boldsymbol{e}_{\text{local}}$ vector field representing the local characteristic direction of the penetrating vessels (a). The first diagonal component of the arteriole or the venule permeability tensor adjusted using the $\boldsymbol{e}_{\text{local}}$ field (b).

2.3 Model parameters

The haemodynamics model governed by equation (1) includes thirty-one parameters: the coupling coefficients in grey (β^G_{ac} & β^G_{cv}) and white matters (β^W_{ac} & β^W_{cv}), and the twenty-seven components of the permeability tensors of each compartment ($\boldsymbol{K_a}$, $\boldsymbol{K_c}$, $\boldsymbol{K_v}$). The permeability tensors and the coupling coefficients of the porous model need to represent the complex structure of the microvasculture with strong preferences regarding arteriole and venule vessel orientation as shown in Figure 1. Therefore, the components of $\boldsymbol{K_a}$, $\boldsymbol{K_c}$, $\boldsymbol{K_v}$ are space-dependent functions.

Penetrating vessels, including Descending Arterioles (DAs) and Ascending Veins (AVs), in the cortex tend to be aligned normal to the pial surface. Consequently, the permeability tensors of the arteriole and venule compartments are similar but anisotropic and inhomogeneous. On the contrary, the permeability tensor of the capillary comparment is isotropic and effectively diagonal. Therefore, the capillary permeability in the grey matter can be described by a single scalar: $k_c = 4.28\times10^{-4}$ [mm^3 s kg^{-1}] [16]. For simplicity we use some assumptions first proposed by [20]: (i) the permeabilities are the same in grey and white matters; (ii) $\boldsymbol{K_v} = 2\boldsymbol{K_a}$; and (iii) the ratio of the grey and white matter coupling coefficients is constant:

$$C_\beta = \frac{\beta^G}{\beta^W} = \frac{\beta^G_{ac}}{\beta^W_{ac}} = \frac{\beta^G_{cv}}{\beta^W_{cv}}. \tag{7}$$

Thereafter, the model is determined by twelve parameters: β^G_{ac}, β^G_{cv}, C_β, and $\boldsymbol{K_a}$.

2.3.1 Permeability tensors

Permeabilities are characterised in a reference Cartesian coordinate system defined by ξ, η, ζ corresponding to a cortical column as shown in Figure 1(b). The $\boldsymbol{e}_{\text{ref}} = [0, 0, 1]$ unit vector defined in the reference coordinate system is parallel to the axes of the penetrating vessels (Figure 1(b)). The arteriole and the venule compartments encapsulate the zeroth order penetrating vessel branches. These major penetrating branches in a cortical column can be imagined as a "vessel bundle" supporting flow only in the ζ direction. For this reason, we assume that the arteriole and venule permeabilities in the reference coordinate system are

$$\boldsymbol{K}^{\text{ref}}_{\boldsymbol{a}} = \begin{bmatrix} 0 & 0 & 0 \\ 0 & 0 & 0 \\ 0 & 0 & k_a \end{bmatrix}, \quad \text{and} \quad \boldsymbol{K}^{\text{ref}}_{\boldsymbol{v}} = \begin{bmatrix} 0 & 0 & 0 \\ 0 & 0 & 0 \\ 0 & 0 & k_v \end{bmatrix}. \tag{8}$$

In this formulation, every higher order arteriole and venule side branch is lumped into a conductance represented by the coupling coefficients.

This approach includes numerous simplifications but it has three advantages. Firstly, the permeability of a "vessel bundle" with laminar flow within (k_{vb}) can be estimated as

$$k_a \approx k_{vb} = \frac{n_v D^4 \pi}{128 \mu_b A_{\text{ref}}}. \tag{9}$$

Here, D is the characteristic diameter of the vessels and n_v is the number of vessels corresponding to a reference cortical surface area A_{ref}. The *in vitro* dynamic viscosity of blood (μ_b) depends on the diameter and the haematocrit as described in [44]. Assuming a constant discharge haematocrit of 45%, a mean diameter in the range of $D = 50 - 90$ microns [45, 46] with $n_v = 8$ PAs per $A_{\text{ref}} = 1$ mm^2 [47, 17] leads to $k_a/k_c = 1000 - 10000$. The final value of k_a is optimised with an initial guess within this range. This optimisation is presented in Section 3.1.

Secondly, in the reference coordinate the permeability tensor has a single-valued element (instead of space-dependent functions). Thirdly, once a permeability tensor is determined in a reference coordinate system ($\boldsymbol{K}_{\boldsymbol{i}}^{\text{ref}}$) with a given reference direction ($\boldsymbol{e}_{\text{ref}}$), the permeability tensor (function) $\boldsymbol{K_i}$ can be computed as detailed in Appendix A. The unit vector corresponding to the local characteristic direction is given as

$$\boldsymbol{e}_{\text{local}} = \nabla a / |\nabla a|, \tag{10}$$

where we define scalar field a that satisfies

$$\nabla^2 a = 0. \tag{11}$$

The boundary conditions are $a = 1$ on Γ_P, $a = 0$ on Γ_{V}, and $\nabla a \cdot \boldsymbol{n} = 0$ on Γ_{BS}.

During angiogenesis penetrating vessels grow to perfuse deeper brain regions. It is hypothesised that vessels grow following the path of least resistance path from the cortical surface to the ventricles which is indicated by the computed $\boldsymbol{e}_{\text{local}}$ field. Hence, it is assumed that the $\boldsymbol{e}_{\text{local}}$ vectors visualised in Figure 4(a) indicate the local direction of the penetrating vessel axes. The permeability tensors of the arteriole and venule compartments are rotated to support blood flow only parallel to $\boldsymbol{e}_{\text{local}}$. The first diagonal component of the normalised arteriole permeability tensor is depicted in Figure 4(b). High values of K_{11} indicate regions where blood flow in the arterioles and the venules is supported primarily in the lateral direction. Where K_{11} is relatively low, blood flow occurs mostly along the distal-proximal and the anterior-posterior directions.

2.3.2 Coupling coefficients

The coupling coefficients are tuned to account for the side branches of the penetrating arterioles and venules. These side branches are referred to as PreCapillaries (PrC) and PostCapillaries (PoC) associated with β_{ac} and β_{cv} respectively. In order to estimate these parameters, the volume-averaged pressure fields are linked to the coupling coefficients.

Integrating equations (1a)-(1c) over Ω_G, applying the divergence theorem, and dividing by the total volume of the grey matter (V_G) leads to the following algebraic equation set.

$$-\frac{Q_a^G}{V_G} - \beta_{ac}^G(\langle p_a \rangle^G - \langle p_c \rangle^G) = 0; \tag{12a}$$

$$-\frac{Q_c^G}{V_G} + \beta_{ac}^G(\langle p_a \rangle^G - \langle p_c \rangle^G) - \beta_{cv}^G(\langle p_c \rangle^G - \langle p_v \rangle^G) = 0; \tag{12b}$$

$$-\frac{Q_v^G}{V_G} + \beta_{cv}^G(\langle p_c \rangle - \langle p_v \rangle^G) = 0. \tag{12c}$$

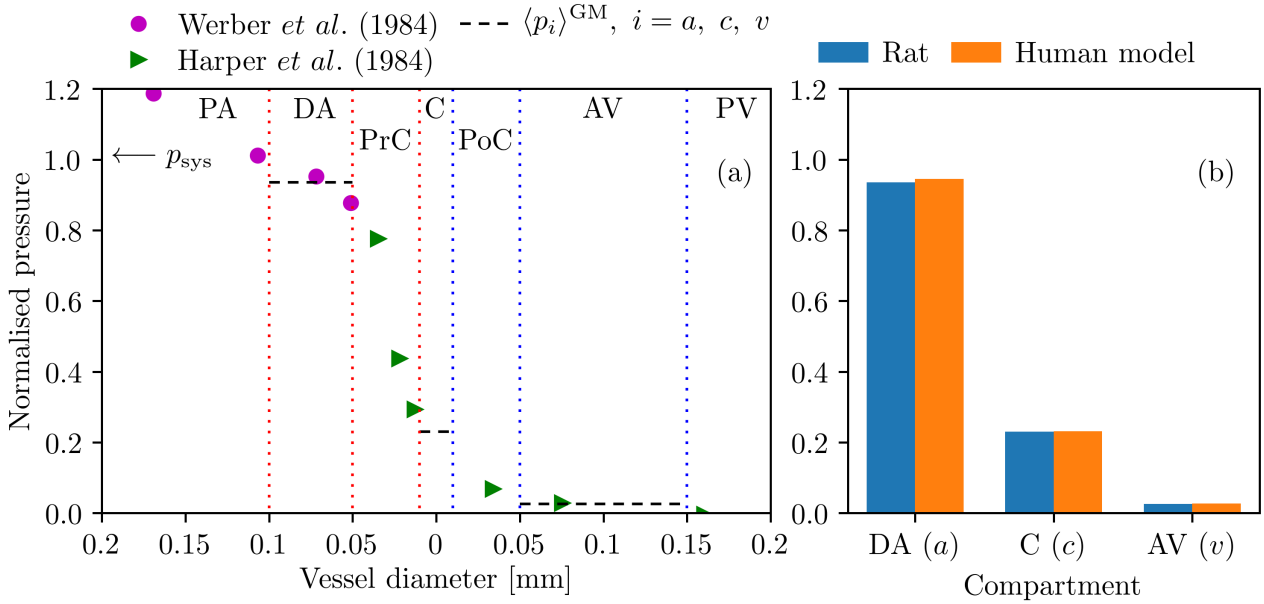

Figure 5: Normalised pressure as a function of the vessel diameter in the grey matter of the rat brain (a). The systolic pressure is used for normalisation. The dotted lines represent theoretical boundaries between the Pial Arteries (PA), Descending Arterioles (DA), PreCapillaries (PrC), Capillaries (C), PostCapillaries (PoC), Ascending Venules (AV), and Pial Veins (PV). The dashed lines represent the hypothetical average pressure values in each compartment. Average pressure in the arteriole, capillary and the venule compartments in the grey matter of the rat brain and the present virtual human brain (b).

Here, the angle brackets denote volume-averaged quantities so that $\langle p_i \rangle^G$ is the average Darcy pressures in the grey matter in compartment i. Furthermore, Q_i^G is the volumetric flow rate through the surface bounding the grey matter in compartment i, defined as

$$Q_i^G = -\iint_{\Gamma_G} \boldsymbol{K_i} \nabla p_i \cdot \mathrm{d}\boldsymbol{A}. \tag{13}$$

In the above expression Γ_G and $\boldsymbol{A}$ symbolise the surface bounding the grey matter and the corresponding area vector respectively.

Given that $k_a/k_c = 1000-10000$, as estimated in Section 2.3.1, Q_c^G/V_G is negligible compared to Q_a^G/V_G and Q_v^G/V_G. According to the imposed boundary conditions, equations (2) and (3), $Q_c^G/V_G \approx 0$ can be assumed which indicates that blood flow in the capillaries through the interface of grey and white matter is comparatively low. This assumption has been used previously in blood flow simulations of cortical columns [16, 18]. Based on equation (12), it thus follows that grey matter perfusion is

$$F^G = -\frac{Q_a^G}{V_G} = \beta_{ac}^G(\langle p_a \rangle^G - \langle p_c \rangle^G) = \beta_{cv}^G(\langle p_c \rangle^G - \langle p_v \rangle^G). \tag{14}$$

In addition, it can be concluded that the ratio of the arteriole-capillary (β_{ac}) and the capillary-venule (β_{cv}) coupling coefficients is related to the volume-averaged pressure drops as

$$\frac{\beta_{ac}^G}{\beta_{cv}^G} = \frac{\langle p_c \rangle^G - \langle p_v \rangle^G}{\langle p_a \rangle^G - \langle p_c \rangle^G}. \tag{15}$$

Therefore, the average perfusion and inter-compartment pressure drops in the grey matter uniquely determine the coupling coefficients β_{ac}^G and β_{cv}^G.

In order to calculate the coupling coefficient in the grey matter, perfusion is calculated from cerebral blood flow set to $Q^{\text{brain}} = 600$ [ml/min] [48]. The total volume of the brain model is $V_{\text{brain}} = 1390$ [ml] which leads to a physiologically realistic brain perfusion $F^{\text{brain}} \approx 43$ [(ml blood)/min/(100 ml tissue)]. The mean ratio of grey and white matter perfusion is $F^G/F^W = 2.7$ [49]. With the grey and white matter volumes given ($V^G = 894$ and $V^W = 496$ [ml]), grey and white matter perfusion values are $F^G \approx 56$ and $F^W \approx 21$ [ml/min/(100 ml)] respectively. The brain volume [50] and perfusion values [49, 38, 28] are in good agreement with the literature.

Pressure measurements in the human microcirculation are not available but experiments have been reported in the rat brain [51, 52]. Based on the summary of these experiments provided by Schmid *et al.* [53], some normalised experimental results are shown in Figure 5(a). $\beta_{cv}/\beta_{ac} = 3.5$ is infered from the ratio of the average pressure drop in each compartment of the rat brain. It is worth mentioning that simulations of the rat brain indicate significant variation of the pressure ratios in different cortical layers [53]. Finally, the systolic pressure in the human brain is set to $p_{\text{sys}} = 75$ mmHg $\approx 10^4$ Pa. (This value is relative to the venous pressure selected as the zero level of the pressure.) According to the calculated grey matter perfusion, the pressure ratios visualised in Figure 5(a) and the systolic pressure value, the coupling coefficients in grey matter are $\beta^G_{ac} = 1.326 \cdot 10^{-6}$ and $\beta^G_{cv} = 4.641 \cdot 10^{-6}$ [1/Pa/s]. Figure 5(b) demonstrates that with these coupling coefficients, the normalised inter-compartment pressure drop of the human brain model is similar to that of the rat brain. Finally, $C_\beta = \beta^G/\beta^W$ can be estimated analytically by rewriting equation (14) for the white matter and assuming that the inter-compartment pressure drop in white matter is the same as in grey matter: $F^G/F^W = \beta^G/\beta^W = 2.7$.

2.4 Numerical procedure

Compared to former finite volume implementations [19, 20], the finite element environment can be advantageous when multi-physics problems are considered. For example, modelling oedema requires handling fluid flow and solid deformation [11]. It has been demonstrated that the finite element method can be utilised efficiently to model such complex physical problems in human organs [54, 55, 56, 57, 58, 24]. For this reason, the governing partial differential equations are solved numerically using Python with a high performance open source finite element library, FEniCS [59, 60]. The weak form of equation (1) is available in [21] and in Appendix B. The equation set is solved in a mixed space covering the full system. The pressure in each compartment (p_i) is discretised using piecewise linear Lagrange (P_1) elements. (The "periodic table" of finite elements can be found in [61].) The permeabilities ($\boldsymbol{K_i}$) and the coupling coefficients (β_{ij}) are represented in (discontinous) piecewise constant (dP_0) tensor and scalar function spaces respectively. This helps to capture the sharp change in the model parameters between the grey and white matters.

The a scalar in the Poisson equation (11) is stored in second-order piecewise polynomial Lagrange (P_2) elements. Therefore, $\boldsymbol{e}_{\text{local}}$ in equation (10) has to be projected from P_1 to dP_0 elements before it is used for the coordinate transformation of $\boldsymbol{K}_{\boldsymbol{i}}^{\text{ref}}$. Finally, tissue perfusion $F = \beta_{ac}(p_a - p_c)$ is computed in dP_0 elements. The resulting linear equation systems are solved iteratively using the BiCojungate Gradient STABilised method (BiCGSTAB) [62]. Pressure field computation is speeded up with an Algebraic MultiGrid (AMG) preconditioner [63]. Adjusting the permeability field and computing the pressure and perfusion fields for the healthy and occluded scenarios take approximately 5 minutes using a single core on a modern desktop equipped with an Intel Xeon E-2146G processor. Exploiting the native Massage Passing Interface (MPI) implementation of FEniCS and running the simulations with two and four cores reduce the wall time to approximately 3 and 2 minutes respectively.

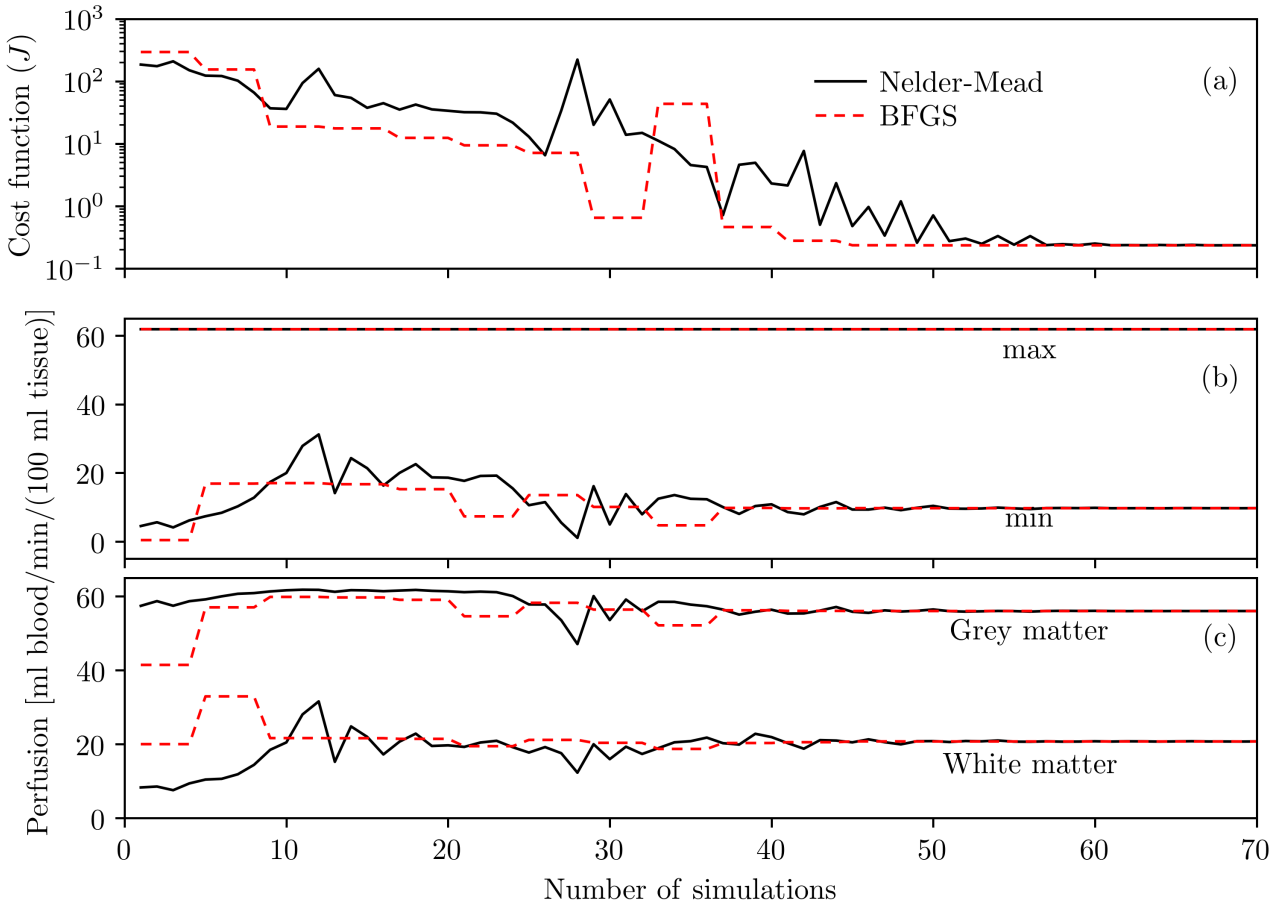

Figure 6: Convergence of the cost function J (a), minimum and maximum perfusion values (b), grey matter and white matter perfusion values (c) as a function of the number of simulation throughout the optimisation.

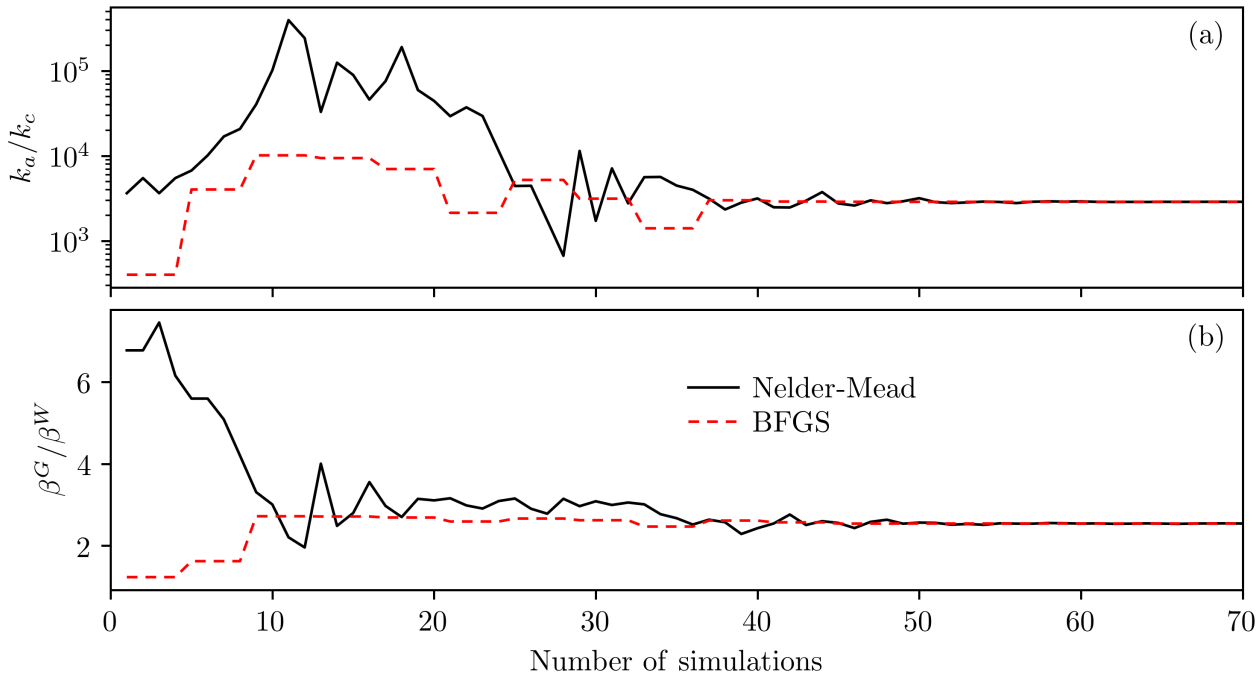

Figure 7: Convergence of the arteriole permeability (a) and the coupling coefficient ratio (b) during the optimisation.

3 Results and discussion

3.1 Parameter optimisation

It turns out that without the simplifications listed in Section 2, it is challenging to pose an optimisation problem with well-distinguished global or local minimum for the complete set of thirty-one parameters. For this reason, the parameter space of the imposed problem is reduced significantly according to Sections 2.3.1 and 2.3.2 and the remaining parameters are optimised.

The optimisation goal is to obtain physiologically accurate average perfusion values for the grey and white matters, hence the cost function (J) to be minimised is

$$J = (F^G - F^G_{\text{target}})^2 + (F^W - F^W_{\text{target}})^2 + J_{\text{penalty}}. \tag{16}$$

The target values are calculated as detailed in Section 2.3.2 and set to $P^G_{\text{target}} \approx 56$ and $P^W_{\text{target}} \approx 21$ [(ml blood)/min/(100 ml tissue)]. Furthermore, a penalty term (J_{penalty}) has been added to restrict the minimum and maximum perfusion values:

$$\begin{aligned} J_{\text{penalty}} =& H(F_{\text{min,target}} - F_{\text{min}}) \cdot (F_{\text{min}} - F_{\text{min,target}})^2 + \\ & H(F_{\text{max}} - F_{\text{max,target}}) \cdot (F_{\text{max}} - F_{\text{max,target}})^2. \end{aligned} \tag{17}$$

Here, H is the Heaviside function resulting in a non-zero J_{penalty} only if the extrema are out of the $P_{\text{min,target}} = 10$ and the $P_{\text{max,target}} = 80$ [(ml blood)/min/(100 ml tissue)] range.

The two remaining parameters are defined as

$$k_a/k_c = 10^p \quad \text{and} \quad C_\beta = \beta^G/\beta^W = 10^q, \tag{18}$$

to restrict the search for positive values. Finally, the two-dimensional optimisation problem can be phrased as

$$\min\left[J(p,q)\right] \quad \text{in} \quad p \in [-\infty, \infty] \text{ and } q \in [-\infty, \infty]. \tag{19}$$

The parameters are initialised randomly within the $p \in [3,4]$ and $q \in [0,1]$ intervalls. The bounding values are estimated according to Sections 2.3.1 and 2.3.2. To find the global minimum

Parameter	Value	Unit
k_a	1.234	$\mathrm{mm}^3\ \mathrm{s}\ \mathrm{kg}^{-1}$
k_c	4.28×10^{-4}	$\mathrm{mm}^3\ \mathrm{s}\ \mathrm{kg}^{-1}$
k_v	2.468	$\mathrm{mm}^3\ \mathrm{s}\ \mathrm{kg}^{-1}$
β_{ac}^G	1.326×10^{-6}	Pa/s
β_{cv}^G	4.641×10^{-6}	Pa/s
β_{ac}^W	5.22×10^{-7}	Pa/s
β_{cv}^W	1.828×10^{-6}	Pa/s
p_v	0	Pa
p_{sys}	10^4 (75)	Pa (mmHg)

Table 1: List of the model parameters.

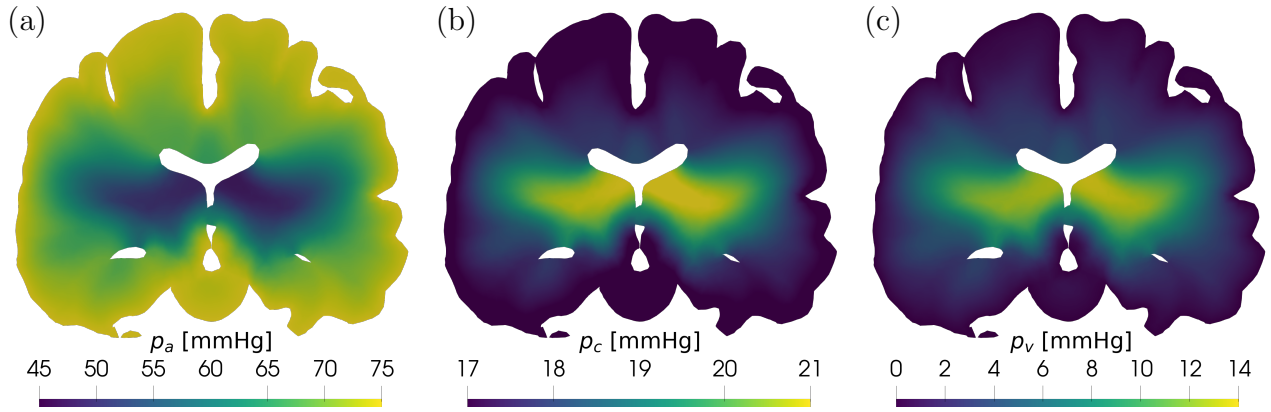

Figure 8: Pressure distribution along the coronal plane shown in Figure 2(c): (a) arteriole, (b) capillary, (c) venule compartment.

of J, the BFGS [64] and the Nelder-Mead [65] methods are employed. Whereas BFGS method relies on computing the derivatives of the cost function, the Nelder-Mead algorithm is gradient-free.

Both algorithms are run three times so that the optimisation problem is solved six times in total to ensure that the obtained parameters are independent of the initial guesses. Every run leads to the same values (with a relatively small tolerance) independently from the initialisation. The cost function and the perfusion values during typical executions are shown in Figures 6(a), (b) and (c). The methods converge to $J \approx 0.2$ within 60 simulations with the minimum, maximum and mean perfusion values reasonably close to the target values. The history of parameters throughout the optimisation can be seen in Figure 7. The final values of the simulation parameters are summarised in Table 1.

3.2 Pressure and perfusion field analysis

Simulations are next performed to model a healthy scenario and a R-MCA occlusion. The pressure field corresponding to the healhty scenario is displayed in Figure 8. A high pressure drop can be observed in the vicinity of the cortical surface in the arteriole compartment which decreases rapidly as white matter is reached. The majority of the pressure drop takes place in the arteriole compartment and between the arteriole and the capillary compartments. The pressure change within the capillary and the venule compartments are relatively small. The volume-averaged pressure values are listed in Table 2.

The resulting perfusion distribution within the brain is visualised in Figure 9. Perfusion within the grey and white matters appear to be uniform. The corresponding mean and stan-

Variable	Healthy	R-MCA occlusion	Healthy reference	
			Female	Male
$\langle p_a \rangle$	9242	7110	6335 [52]	
$\langle p_c \rangle$	2348	1810	1564 [51]	
$\langle p_v \rangle$	379	196	179 [51]	
F^{brain}	43 ± 18	34 ± 24	62 ± 7 [49]	53 ± 10 [49]
F^G	56 ± 6	44 ± 23	68 ± 10 [49]	58 ± 13 [49]
F^W	21 ± 3	16 ± 9	25 ± 5 [49]	23 ± 3 [49]

Table 2: Comparison of integral variables with literature data. The units of pressure and perfusion values are Pa and (ml blood)/min/(100 ml tissue) respectively. Healthy reference pressure is calculated from experimental data on the rat brain as presented in Figure 5. Perfusion is listed as mean ± standard deviation. Standard deviation computed for the simulations describe spatial variation within the virtual brain. The standard deviation corresponding to the reference values represent variation between individuals.

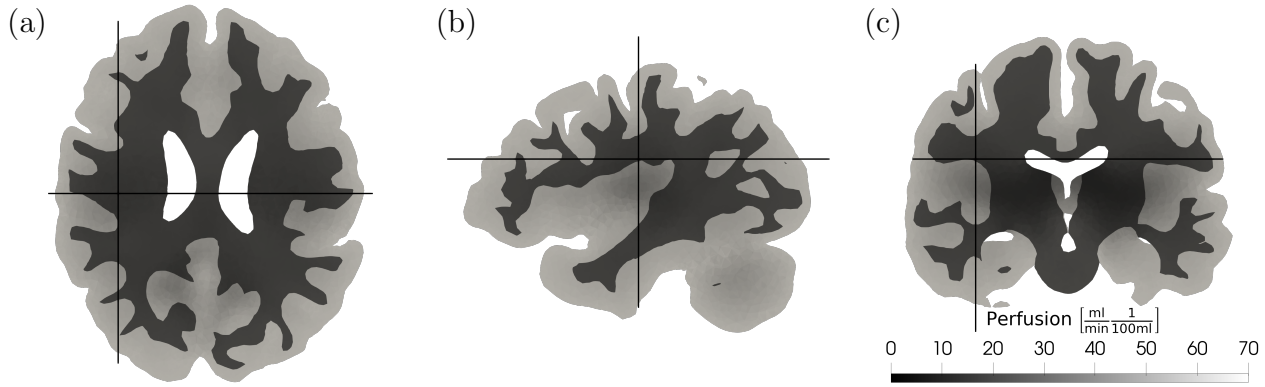

Figure 9: Perfusion distribution along the transverse (a), sagittal (b), and coronal (c) planes shown in Figure 2(c). The solid lines show the location of the slices.

dard deviation values listed in Table 2 are in satisfactory agreement with experimental values obtained from ASL and PET images [49, 38, 28]. The perfusion values in the healthy scenario are representative of an elderly male patient because of the relatively low values. The standard deviation of perfusion within the brain is somewhat higher than the reference values. The difference is probably due to the fact that the simulation values correspond to a spatial integration whereas the standard deviation of experimental values quantify the difference between patients. It is important to emphasise that the model is steady state. For this reason, spatial variations typical of the grey matter due to time-dependent activations are not visible.

Finally, the relative change of tissue perfusion is analysed following the occlusion of the right middle cerebral artery. The occluded scenario is modelled by lowering the pressure at the pial surface region corresponding to the right middle cerebral artery ($p_a \downarrow$ at $\Gamma_{\text{R-MCA}}$). The modified boundary conditions are governed by equation (6). Perfusion change is defined as

$$\text{Perfusion change} = 100\% \left(\frac{F_{\text{occluded}} - F_{\text{healthy}}}{F_{\text{healty}}} \right), \tag{20}$$

so that 0% stands for unchanged perfusion and -100% highlights regions with zero perfusion. As the pressure difference between the arteriole and the venous compartment is lowered, it is expected that an underperfused region appears in the vicinity of $\Gamma_{\text{R-MCA}}$. The penetrating vessels deliver blood from the pial surface to the deep brain regions (see Figure 1). Therefore, the extent of the underperfused region after R-MCA occlusion is determined by the orientation

of the penetrating vessels shown in Figure 4(a).

An underperfused region predicted by the model covering almost the entirety of the right hemisphere can be seen in Figures 10 (a)-(c). Blood flow in the left hemisphere and the cerebellum are not influenced because these regions are perfused by different arteries. Although the human vasculature has compensatory mechanisms and structures to improve survival chance in the case of stroke, for example collateral arteries, it should be noted that these are not included in the model. Therefore, the simulations are capable of predicting only worse case scenarios. Collateral flow is often associated with leptomeningeal arteries with relatively large diameters, therefore this feature could be included in the network model encapsulating the large arteries [14, 15], even though the details of these vessels remain to be explored. It is interesting to see that the strongly interconnected capillary vessels cannot balance such a drastic loss of blood inflow. Due to its high resistance, a static capillary network simply cannot compensate major perfusion losses.

In Figures 10 (d)-(f), follow-up non-contrast CT scan images of a 76-year-old male patient are presented. This patient arrived at the hospital four hours after stroke symptom onset. The CT angiography on hospital admission showed a proximal occlusion of the right M1-segment (mother branch) of the MCA and poor collaterals (only very few vessels visible in the occluded vascular territory compared to the asymptomatic contralateral hemisphere). The patient presented at the hospital with a severe stroke-related neurologic deficit according to the National Institutes of Health Stroke scale. After diagnostic workup, the patient arrived at the angiosuite for thrombectomy approximately five hours after stroke onset. The follow-up CT scans in Figures 10 (d)-(f) show severe hypodensity of the right MCA territory one week after treatment associated with an acute infarct.

The infarcted region in Figures 10 (d)-(f) is in satisfactory qualitative agreement with the low perfusion regions in Figures 10 (a)-(c). The results suggest that virtual perfusion maps are suitable to predict infarct location but that capturing the extent of the infarct quantitatively is more challenging. Even though the formation and expansion of an infarction core is clearly linked to the lack of perfusion, necrosis is driven by the lack of nutritions in general. Tissue metabolism relies on oxygen and glucose, therefore it is essential to capture the advective-diffusive transport of these substances when it comes to the accurate prediction of the infarct volume.

3.3 Limitations

This subsection aims to summarise some factors which have been overlooked in the present study. Firstly, fast, reliable and accurate automatised patient-specific mesh generation remains a major challenge. For this reason, the present study is limited to a single patient-specific geometry. Organ-scale models have a great potential to ease clinical decision making and improve treatment but user-friendly and automatised pipelines need to be implemented. One of the major stumbling block of automatisation is patient-specific mesh generation based on medical images.

Secondly, the presented multi-compartment porous model relies on multiple scale separation. It has been pointed out that the vessel diameter in the vasculature changes continously therefore the applicability of scale separation is questionable [18]. The present study demonstrated promising but solely qualitative validation of this approach using medical images. The next stage of validation is to conduct a large set of simulations and evaluate the accuracy of predictions in comparison to medical images.

Thirdly, estimating the parameters of human physiological models has always been a difficult task because of the lack of sufficient data. The present optimisation relies on numerous simplifications listed in Section 2. These assumptions have been used previously [20] and are

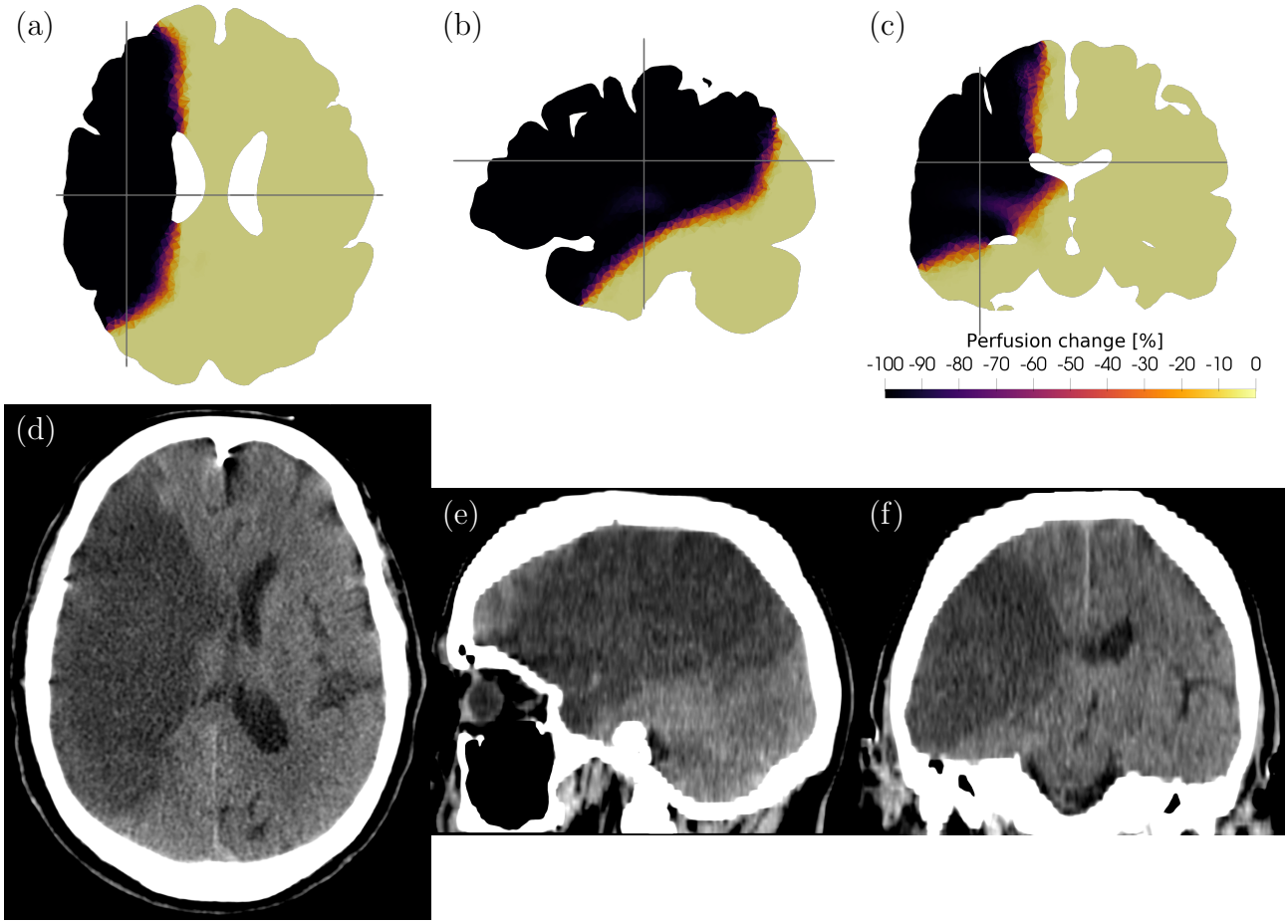

Figure 10: Relative change of perfusion as a result of a total blockage of the right middle cerebral artery (R-MCA). The perfusion change is visualised along the transverse (a), sagittal (b), and coronal (c) planes shown in Figure 2(c). The solid lines show the location of the slices. CT images of a patient with a similar occlusion along the same transverse (d), sagittal (e), and coronal (f) planes.

sufficient to test models but they have not been thoroughly justified. Providing a more careful evaluation of the permeabilies and coupling coefficients in the grey matter based on statistically accurate network models of the microcirculation [66, 16, 46] is work in progress.

Finally, the following features have been neglected and are targets of future model expansion: cerebral autoregulation [43], oedema [11], emboli advection and blockage of the microcirculation [9, 10], spreading of ischaemic tissue damage [67, 68], etc. These phenomena are time-dependent and often rely on nonlinear processes. Modelling these features and capturing their interaction could provide valuable new insights but due to their extreme complexity their description is beyond the scope of the present study.

4 Conclusions

This study has investigated the capabilities of a three-compartment porous microcirculation model for perfusion predictions in healthy humans as well as in ischaemic stroke patients. Inspired by advances in organ-scale human heart [54, 55, 56, 24] and lung modelling [57, 58], we aimed to lay down the fundamentals of a software suite which will facilitate a model environment for multi-scale and multi-physics simulations of the human brain. For this reason, the finite element method has been utilised in contrast with former studies which preferred the finite volume method [19, 20].

An anatomically accurate mapping between large arteries and microvessels has been introduced. We have utilised vessel-encoded arterial spin labelling data and a novel clustering algorithm previously developed in our group to identify superficial cortical perfusion territories. A robust approach has been proposed to account for heterogeneity and anisotropy in the microcirculation of the human brain using permeability tensors. To obtain the resulting parameters, optimisation has been combined with parameter space reduction based on the analysis of the governing equations and experimental data.

Simulations have been conducted to predict perfusion in both a healthy and an occluded scenario. A right middle cerebral artery occlusion has been implemented for which CT images have also been presented. The occlusion resulted in a drastic perfusion drop impacting most of the right hemisphere. A satisfactory qualitative agreement has been found between the infarcted region visible in the CT images and the low perfusion region predicted by the simulations.

In the future, the model will be coupled to a one-dimensional network model of the large arteries [14, 15] to create a complete *in silico* cerebral circulation model. Thereafter, the model will be validated using a large set of clinical data, such as CT perfusion images, which will also help to tune model parameters and improve accuracy. In order to predict infarct formation and propagation during ischaemic stroke, metabolism-based dynamic models will be developed.

Acknowledgement

This project has received funding from the European Union's Horizon 2020 research and innovation programme. Thanks are due to the members of the INSIST consortium for useful discussions and their sustained support. T. I. Józsa is grateful to H. J. M. M. Mutsaerts of Amsterdam UMC, T. W. Okell and M. A. Chappell of the Universty of Oxford for sharing arterial spin labelling data and suggesting efficient application routes. T. I. Józsa also wishes to thank Patrick Farrell of the University of Oxford for his insightful suggestions regarding parameter optimisation.

A Transformation matrix calculation

The permeability $\boldsymbol{K}_{\boldsymbol{a}}^{\mathrm{ref}}$ is given in the reference coordinate system defined by $\boldsymbol{e}_{\mathrm{ref}}$ as detailed in Section 2.3.1. Furthermore, $\boldsymbol{e}_{\mathrm{local}}$ is a vector field computed according to equations (10) and (11). The local permeability tensor is obtained from $\boldsymbol{K_i} = \boldsymbol{R}\boldsymbol{K}_{\boldsymbol{i}}^{\mathrm{ref}}\boldsymbol{R}^{\mathrm{T}}$. Here, $\boldsymbol{R}$ is the transformation tensor which can be calculated as follows [69]. The unit vector defining the axis of rotation is

$$\boldsymbol{e}_{\mathrm{rot}} = \frac{\boldsymbol{e}_{\mathrm{ref}} \times \boldsymbol{e}_{\mathrm{local}}}{|\boldsymbol{e}_{\mathrm{ref}} \times \boldsymbol{e}_{\mathrm{local}}|}. \tag{21}$$

The rotation angle θ can be calculated as $\cos^{-1}(\boldsymbol{e}_{\mathrm{ref}} \cdot \boldsymbol{e}_{\mathrm{local}})$ and the cross product matrix of $\boldsymbol{e}_{\mathrm{rot}}$ is defined as

$$[\boldsymbol{e}_{\mathrm{rot}}]_{\times} = \begin{bmatrix} 0 & -e_{\mathrm{rot},3} & e_{\mathrm{rot},2} \\ e_{\mathrm{rot},3} & 0 & -e_{\mathrm{rot},1} \\ -e_{\mathrm{rot},2} & e_{\mathrm{rot},1} & 0 \end{bmatrix}. \tag{22}$$

Here, $e_{\mathrm{rot},i}$ is the i^{th} component of $\boldsymbol{e}_{\mathrm{rot}}$. Finally, the transformation matrix can be expressed as

$$\boldsymbol{R} = \cos(\theta)\boldsymbol{I} + \sin(\theta)\,[\boldsymbol{e}_{\mathrm{rot}}]_{\times} + [1 - \cos(\theta)]\,(\boldsymbol{e}_{\mathrm{rot}} \otimes \boldsymbol{e}_{\mathrm{rot}}), \tag{23}$$

where $\boldsymbol{I}$ denotes the identity matrix.

B Weak form of the governing equations

The governing equation set and the imposed boundary conditions are equations (1) and (2)–(6) respectively. The weak form can be derived by taking the volume integral of equations (1a)–(1b). Thereafter, integration by parts and the application of the divergence theorem result in

$$\int_{\Omega} (\boldsymbol{K_a} \cdot \nabla p_a) \cdot (\nabla v_a)\,\mathrm{d}\Omega = -\int_{\Omega} \beta_{ac}(p_a - p_c)v_a \mathrm{d}\Omega; \tag{24a}$$

$$\int_{\Omega} (\boldsymbol{K_c} \cdot \nabla p_c) \cdot (\nabla v_c)\,\mathrm{d}\Omega = \int_{\Omega} \beta_{ac}(p_a - p_c)v_c \mathrm{d}\Omega - \int_{\Omega} \beta_{cv}(p_c - p_v)v_c \mathrm{d}\Omega; \tag{24b}$$

$$\int_{\Omega} (\boldsymbol{K_v} \cdot \nabla p_v) \cdot (\nabla v_v)\,\mathrm{d}\Omega = \int_{\Omega} \beta_{cv}(p_c - p_v)v_v \mathrm{d}\Omega. \tag{24c}$$

In the above expression, v_i denotes the test function of compartment i.

References

[1] D. S. Liebeskind. Reperfusion for acute ischemic stroke: arterial revascularization and collateral therapeutics. *Current Opinion in Neurology*, 23(1):36–45, 2010.

[2] P. S. S. Fransen, D. Beumer, O. A. Berkhemer, L. A. van den Berg, H. Lingsma, A. van der Lugt, W. H. van Zwam, R. J. van Oostenbrugge, Y. B. W. E. M. Roos, C. B. Majoie, et al. MR CLEAN, a multicenter randomized clinical trial of endovascular treatment for acute ischemic stroke in the Netherlands: study protocol for a randomized controlled trial. *Trials*, 15(1):343, 2014.

[3] O. A. Berkhemer, P. S. S. Fransen, D. Beumer, L. A. van den Berg, H. F. Lingsma, A. J. Yoo, W. J. Schonewille, J. A. Vos, P. J. Nederkoorn, M. J. H. Wermer, et al. A randomized trial of intraarterial treatment for acute ischemic stroke. *New England Journal of Medicine*, 372(1):11–20, 2015.

[4] O. O. Seminog, P. Scarborough, F. L. Wright, M. Rayner, and M. J. Goldacre. Determinants of the decline in mortality from acute stroke in England: linked national database study of 795 869 adults. *British Medical Journal*, 365:l1778, 2019.

[5] E. S. Donkor. Stroke in the 21(st) Century: A Snapshot of the Burden, Epidemiology, and Quality of Life. *Stroke Research and Treatment*, 2018, 2018.

[6] J. M. Veerbeek, G. Kwakkel, E. E. H. van Wegen, J. C. F. Ket, and M. W. Heymans. Early prediction of outcome of activities of daily living after stroke: a systematic review. *Stroke*, 42(5):1482–1488, 2011.

[7] C. Iadecola. The neurovascular unit coming of age: a journey through neurovascular coupling in health and disease. *Neuron*, 96(1):17–42, 2017.

[8] F. Cassot, F. Lauwers, C. Fouard, S. Prohaska, and V. Lauwers-Cances. A novel three-dimensional computer-assisted method for a quantitative study of microvascular networks of the human cerebral cortex. *Microcirculation*, 13(1):1–18, 2006.

[9] V. J. Marder, D. J. Chute, S. Starkman, A. M. Abolian, C. Kidwell, D. Liebeskind, B. Ovbiagele, F. Vinuela, G. Duckwiler, R. Jahan, P. M. Vespa, S. Selco, V. Rajajee, D. Kim, N. Sanossian, and J. L. Saver. Analysis of thrombi retrieved from cerebral arteries of patients with acute ischemic stroke. *Stroke*, 37(8):2086–2093, 2006.

[10] F. Bajd and I. Sersa. Mathematical modeling of blood clot fragmentation during flow-mediated thrombolysis. *Biophysical Journal*, 104(5):1181 – 1190, 2013.

[11] J. C. Vardakis, D. Chou, B. J. Tully, C. C. Hung, T. H. Lee, P.-H. Tsui, and Y. Ventikos. Investigating cerebral oedema using poroelasticity. *Medical Engineering & Physics*, 38(1):48 – 57, 2016.

[12] D. J. Gladstone, S. E. Black, and A. M. Hakim. Toward wisdom from failure - Lessons from neuroprotective stroke trials and new therapeutic directions. *Stroke*, 33(8):2123–2136, 2002.

[13] A. G. Hoekstra, E. van Bavel, M. Siebes, F. Gijsen, and L. Geris. Virtual physiological human 2016: translating the virtual physiological human to the clinic. *Interface Focus*, 8, 2016.

[14] R. M. Padmos, T. I. Józsa, W. K. El-Bouri, S. J. Payne, and A. G. Hoekstra. Connecting arterial blood flow to tissue perfusion for in silico trials of acute ischaemic stroke. In *CompBioMed Conference, 25-27 September*, 2019.

[15] R. M. Padmos, T. I. Józsa, W. K. El-Bouri, S. J. Payne, and A. G. Hoekstra. Coupling arterial blood flow to tissue perfusion models for in silico trials of acute ischaemic stroke. *Interface Focus*, page (under review), 2019.

[16] W. K. El-Bouri and S. J. Payne. Multi-scale homogenization of blood flow in 3-dimensional human cerebral microvascular networks. *Journal of Theoretical Biology*, 380:40–47, 2015.

[17] W. K. El-Bouri and S. J. Payne. Investigating the effects of a penetrating vessel occlusion with a multi-scale microvasculature model of the human cerebral cortex. *NeuroImage*, 172:94–106, 2018.

[18] M. Peyrounette, Y. Davit, M. Quintard, and S. Lorthois. Multiscale modelling of blood flow in cerebral microcirculation: Details at capillary scale control accuracy at the level of the cortex. *PLoS ONE*, 13(1):e0189474, 2018.

[19] S. Blowers, I. Marshall, M. Thrippleton, P. Andrews, B. Harris, I. Bethune, and P. Valluri. How does blood regulate cerebral temperatures during hypothermia? *Scientific Reports*, 8(1):7877, 2018.

[20] E. Hodneland, E. Hanson, O. Sævareid, G. Nævdal, A. Lundervold, V. Šoltészová, A. Z. Munthe-Kaas, A. Deistung, J. R. Reichenbach, and J. M. Nordbotten. A new framework for assessing subject-specific whole brain circulation and perfusion using MRI-based measurements and a multi-scale continuous flow model. *PLoS Computational Biology*, 15(6):e1007073, 2019.

[21] C. Michler, A. N. Cookson, R. Chabiniok, E. Hyde, J. Lee, M. Sinclair, T. Sochi, A. Goyal, G. Vigueras, D. A. Nordsletten, and N. P. Smith. A computationally efficient framework for the simulation of cardiac perfusion using a multi-compartment Darcy porous-media flow model. *International Journal for Numerical Methods in Biomedical Engineering*, 29(2):217–232, 2013.

[22] E. R. Hyde, C. Michler, J. Lee, A. N. Cookson, R. Chabiniok, D. A. Nordsletten, and N. P Smith. Parameterisation of multi-scale continuum perfusion models from discrete vascular networks. *Medical & Biological Engineering & Computing*, 51(5):557–570, 2013.

[23] E. R. Hyde, A. N. Cookson, J. Lee, C. Michler, A. Goyal, T. Sochi, R. Chabiniok, M. Sinclair, D. A. Nordsletten, J. Spaan, J. P. H. M. van den Wijngaard, M. Siebes, and N. P. Smith. Multi-scale parameterisation of a myocardial perfusion model using whole-organ arterial networks. *Annals of Biomedical Engineering*, 42(4):797–811, 2014.

[24] A. Santiago, J. Aguado-Sierra, M. Zavala-Aké, R. Doste-Beltran, S. Gómez, R. Arís, J. C. Cajas, E. Casoni, and M. Vázquez. Fully coupled fluid-electro-mechanical model of the human heart for supercomputers. *International Journal for Numerical Methods in Biomedical Engineering*, 34(12):e3140, 2018.

[25] J. Weickenmeier, M. Jucker, A. Goriely, and E. Kuhl. A physics-based model explains the prion-like features of neurodegeneration in Alzheimers disease, Parkinsons disease, and amyotrophic lateral sclerosis. *Journal of the Mechanics and Physics of Solids*, 124:264–281, 2019.

[26] L. Tatu, T. Moulin, J. Bogousslavsky, and H. Duvernoy. Arterial territories of the human brain: cerebral hemispheres. *Neurology*, 50(6):1699–1708, 1998.

[27] T. W. Okell, M. A. Chappell, M. E. Kelly, and P. Jezzard. Cerebral blood flow quantification using vessel-encoded arterial spin labeling. *Journal of Cerebral Blood Flow & Metabolism*, 33(11):1716–1724, 2013.

[28] H. J. M. M. Mutsaerts, J. W. van Dalen, D. F. R. Heijtel, P. F. C. Groot, C. B. L. M. Majoie, E. T. Petersen, E. Richard, and A. J. Nederveen. Cerebral perfusion measurements in elderly with hypertension using arterial spin labeling. *PloS one*, 10(8):e0133717, 2015.

[29] J. Alastruey, K. H. Parker, J. Peiró, S. M. Byrd, and S. J. Sherwin. Modelling the circle of Willis to assess the effects of anatomical variations and occlusions on cerebral flows. *Journal of Biomechanics*, 40(8):1794–1805, 2007.

[30] K. S. Matthys, J. Alastruey, J. Peiró, A. W. Khir, P. Segers, P. R. Verdonck, K. H. Parker, and S. J. Sherwin. Pulse wave propagation in a model human arterial network: assessment of 1-D numerical simulations against in vitro measurements. *Journal of Biomechanics*, 40(15):3476–3486, 2007.

[31] G. Bárdossy and G. Halász. A "backward" calculation method for the estimation of central aortic pressure wave in a 1D arterial model network. *Computers & Fluids*, 73:134–144, 2013.

[32] T. . Józsa and Gy. Paál. Boundary conditions for flow simulations of abdominal aortic aneurysms. *International Journal of Heat and Fluid Flow*, 50:342–351, 2014.

[33] P. J. Blanco, L. O. Müller, and J. D. Spence. Blood pressure gradients in cerebral arteries: a clue to pathogenesis of cerebral small vessel disease. *Stroke and Vascular Neurology*, 2(3):108–117, 2017.

[34] D. Garcia-Gonzalez, J. Jayamohan, S. N. Sotiropoulos, S.-H. Yoon, J. Cook, C. R. Siviour, A. Arias, and A. Jérusalem. On the mechanical behaviour of PEEK and HA cranial implants under impact loading. *Journal of the Mechanical Behavior of Biomedical Materials*, 69:342–354, 2017.

[35] D. Garcia-Gonzalez, N. S. Race, N. L. Voets, D. R. Jenkins, S. N. Sotiropoulos, G. Acosta, M. Cruz-Haces, J. Tang, R. Shi, and A. Jérusalem. Cognition based bTBI mechanistic criteria; a tool for preventive and therapeutic innovations. *Scientific Reports*, 8(1):10273, 2018.

[36] H. Si. TetGen, a Delaunay-based quality tetrahedral mesh generator. *ACM Transactions on Mathematical Software*, 41(2):11, 2015.

[37] N. S. Hartkamp, E. T. Petersen, J. B. De Vis, R. P. H. Bokkers, and J. Hendrikse. Mapping of cerebral perfusion territories using territorial arterial spin labeling: techniques and clinical application. *NMR in Biomedicine*, 26(8):901–912, 2013.

[38] D. F. R. Heijtel, H. J. M. M. Mutsaerts, E. Bakker, P. Schober, M. F. Stevens, E. T. Petersen, B. N. M. van Berckel, C. B. L. M. Majoie, J. Booij, M. J. P. van Osch, E. van Bavel, R. Boellaard, A. A. Lammertsma, and A. J. Nederveen. Accuracy and precision of pseudo-continuous arterial spin labeling perfusion during baseline and hypercapnia: a head-to-head comparison with ^{15}O H2O positron emission tomography. *NeuroImage*, 92:182–192, 2014.

[39] N. S. Hartkamp, E. T. Petersen, M. A. Chappell, T. W. Okell, M. Uyttenboogaart, C. J. Zeebregts, and R. P. H. Bokkers. Relationship between haemodynamic impairment and collateral blood flow in carotid artery disease. *Journal of Cerebral Blood Flow & Metabolism*, 38(11):2021–2032, 2018.

[40] T. I. Józsa, W. K. El-Bouri, R. M. Padmos, S. J. Payne, and A. G. Hoekstra. A cerebral circulation model for in silico clinical trials of ischaemic stroke. In *CompBioMed Conference, 25-27 September*, 2019.

[41] R. A. Hill, L. Tong, P. Yuan, S. Murikinati, S. Gupta, and J. Grutzendler. Regional blood flow in the normal and ischemic brain is controlled by arteriolar smooth muscle cell contractility and not by capillary pericytes. *Neuron*, 87(1):95–110, 2015.

[42] D. Attwell, A. Mishra, C. N. Hall, F. M. OFarrell, and T. Dalkara. What is a pericyte? *Journal of Cerebral Blood Flow & Metabolism*, 36(2):451–455, 2016.

[43] S. J. Payne. *Cerebral Blood Flow and Metabolism: A Quantitative Approach*. World Scientific, 2017.

[44] A. R. Pries, T. W. Secomb, T. Gessner, M. B. Sperandio, J. F. Gross, and P. Gaehtgens. Resistance to blood flow in microvessels in vivo. *Circulation Research*, 75(5):904–915, 1994.

[45] H. M. Duvernoy, S. Delon, and J. L. Vannson. Cortical blood vessels of the human brain. *Brain Research Bulletin*, 7(5):519–579, 1981.

[46] W. K. El-Bouri and S. J. Payne. A statistical model of the penetrating arterioles and venules in the human cerebral cortex. *Microcirculation*, 23(7):580–590, 2016.

[47] L. Risser, F. Plouraboue, P. Cloetens, and C. Fonta. A 3D-investigation shows that angiogenesis in primate cerebral cortex mainly occurs at capillary level. *International Journal of Developmental Neuroscience*, 27(2):185–196, 2009.

[48] C.-Y. Xing, T. Tarumi, J. Liu, Y. Zhang, M. Turner, J. Riley, C. D. Tinajero, L.-J. Yuan, and R. Zhang. Distribution of cardiac output to the brain across the adult lifespan. *Journal of Cerebral Blood Flow & Metabolism*, 37(8):2848–2856, 2017.

[49] L. M. Parkes, W. Rashid, D. T. Chard, and P. S. Tofts. Normal cerebral perfusion measurements using arterial spin labeling: reproducibility, stability, and age and gender effects. *Magnetic Resonance in Medicine*, 51(4):736–743, 2004.

[50] E. Lüders, H. Steinmetz, and L. Jäncke. Brain size and grey matter volume in the healthy human brain. *Neuroreport*, 13(17):2371–2374, 2002.

[51] S. L. Harper and H. G. Bohlen. Microvascular adaptation in the cerebral cortex of adult spontaneously hypertensive rats. *Hypertension*, 6(3):408–419, 1984.

[52] A. H. Werber and D. D. Heistad. Effects of chronic hypertension and sympathetic nerves on the cerebral microvasculature of stroke-prone spontaneously hypertensive rats. *Circulation Research*, 55(3):286–294, 1984.

[53] F. Schmid, P. S. Tsai, D. Kleinfeld, P. Jenny, and B. Weber. Depth-dependent flow and pressure characteristics in cortical microvascular networks. *PLoS Computational Biology*, 13(2):e1005392, 2017.

[54] J. Relan, P. Chinchapatnam, M. Sermesant, K. Rhode, M. Ginks, H. Delingette, C. A. Rinaldi, R. Razavi, and N. Ayache. Coupled personalization of cardiac electrophysiology models for prediction of ischaemic ventricular tachycardia. *Interface focus*, 1(3):396–407, 2011.

[55] M. Vázquez, R. Arís, G. Houzeaux, R. Aubry, P. Villar, J. Garcia-Barnés, D. Gil, and F. Carreras. A massively parallel computational electrophysiology model of the heart. *International Journal for Numerical Methods in Biomedical Engineering*, 27(12):1911–1929, 2011.

[56] J. Walmsley, J. F. Rodriguez, G. R. Mirams, K. Burrage, I. R. Efimov, and B. Rodriguez. mRNA expression levels in failing human hearts predict cellular electrophysiological remodeling: a population-based simulation study. *PloS one*, 8(2):e56359, 2013.

[57] K. S. Burrowes, J. De Backer, R. Smallwood, P. J. Sterk, I. Gut, R. Wirix-Speetjens, S. Siddiqui, J. Owers-Bradley, J. Wild, D. Maier, C. Brightling, et al. Multi-scale computational models of the airways to unravel the pathophysiological mechanisms in asthma and chronic obstructive pulmonary disease (AirPROM). *Interface Focus*, 3(2):20120057, 2013.

[58] H. Calmet, A. M. Gambaruto, A. J. Bates, M. Vázquez, G. Houzeaux, and D. J. Doorly. Large-scale CFD simulations of the transitional and turbulent regime for the large human airways during rapid inhalation. *Computers in Biology and Medicine*, 69:166–180, 2016.

[59] A. Logg and G. N. Wells. DOLFIN: Automated finite element computing. *ACM Transactions on Mathematical Software*, 37(2):20, 2010.

[60] A. Logg, K.-A. Mardal, and G. Wells. *Automated Solution of Differential Equations by the Finite Element Method: The FEniCS Book*, volume 84. Springer Science & Business Media, 2012.

[61] M. Alnæs, J. Blechta, J. Hake, A. Johansson, B. Kehlet, A. Logg, C. Richardson, J. Ring, M. E. Rognes, and G. N. Wells. The FEniCS project version 1.5. *Archive of Numerical Software*, 3(100), 2015.

[62] H. A. Van der Vorst. Bi-CGSTAB: A fast and smoothly converging variant of Bi-CG for the solution of nonsymmetric linear systems. *SIAM Journal on Scientific and Statistical Computing*, 13(2):631–644, 1992.

[63] Y. Shapira. Multigrid Algorithms. In *Matrix-Based Multigrid*, pages 61–67. Springer, 2003.

[64] C. Zhu, R. H. Byrd, P. Lu, and J. Nocedal. Algorithm 778: L-BFGS-B: Fortran subroutines for large-scale bound-constrained optimization. *ACM Transactions on Mathematical Software)*, 23(4):550–560, 1997.

[65] J. A. Nelder and R. Mead. A simplex method for function minimization. *The Computer Journal*, 7(4):308–313, 1965.

[66] S.-W. Su, M. Catherall, and S. J. Payne. The influence of network structure on the transport of blood in the human cerebral microvasculature. *Microcirculation*, 19(2):175–187, 2012.

[67] E. Ruppin, E. Ofer, J. A. Reggia, K. Revett, and S. Goodall. Pathogenic mechanisms in ischemic damage: a computational study. *Computers in Biology and Medicine*, 29(1):39–59, 1999.

[68] L. Vatov, Z. Kizner, E. Ruppin, S. Meilin, T. Manor, and A. Mayevsky. Modeling brain energy metabolism and function: a multiparametric monitoring approach. *Bulletin of mathematical biology*, 68(2):275–291, 2006.

[69] I. R. Cole. *Modelling CPV*. PhD thesis, Loughborough University, 2015.